Entropy-Driven Incommensurability: Chemical Pressure-Guided Polymorphism in PdBi and the Origins of Lock-in Phenomena in Modulated Systems

Laura C. Folkers[†,◊], Hillary E. Mitchell Warden[‡,◊], Daniel C. Fredrickson[‡,*], Sven Lidin[†,*]

[◊]Equal contributors

[†]Centre for Analysis and Synthesis, Lunds Universitet, Naturvetarvägen 14, 222-61 Sweden

[‡]Department of Chemistry, University of Wisconsin–Madison, 1101 University Avenue, Madison, Wisconsin 53706, United States

ABSTRACT: Incommensurate order, in which two or more mismatched periodic patterns combine to make a long-range ordered yet aperiodic structure, is emerging as a general phenomenon impacting the crystal structures of compounds ranging from alloys and nominally simple salts to organic molecules and proteins. The origins of incommensurability in these systems are often unclear, but it is commonly associated with relatively weak interactions that become apparent only at low temperatures. In this Article, we elucidate an incommensurate modulation in the intermetallic compound PdBi that arises from a different mechanism: the controlled increase of entropy at higher temperatures. Following the synthesis of PdBi, we structurally characterize two low-temperature polymorphs of the TlI-type structure with single crystal synchrotron X-ray diffraction. At room temperature, we find a simple commensurate superstructure of the TlI-type structure (comm-PdBi), in which the Pd sublattice distorts to form a 2D pattern of short and long Pd-Pd contacts. Upon heating, the structure converts to an incommensurate variant (incomm-PdBi) corresponding to the insertion of thin slabs of the original TlI type into the superstructure. Theoretical bonding analysis suggests that comm-PdBi is driven by the formation of isolobal Pd-Pd bonds along shortened contacts in the distorted Pd network, which is qualitatively in accord with the 18–*n* rule but partially frustrated by the population of competing Bi-Bi bonding states. The emergence of incomm-PdBi upon heating is rationalized with the DFT-Chemical Pressure (CP) method: the TlI-type slabs result in regions of higher vibrational freedom that are entropically-favored at higher temperatures. High temperature incommensurability may be encountered in other materials when bond formation is weakened by competing electronic states, and there is a path for accommodating defects in the CP scheme.

1. INTRODUCTION

Incommensurability, in which the positions or occupancy of atoms are modulated with a periodicity decoupled from that of the underlying host lattice, is being recognized in an ever-expanding range of systems spanning from metals,[1] ionic salts,[2,3] alloys,[4,5] geological samples,[6,7] to as far as the crystals of organic molecules[8,9] and the actin protein.[10,11] Alongside intriguing structures, incommensurability offers the possibility for high thermoelectric performance (through lowering thermal conductivity)[12] and non-zero optical activity in centrosymmetric space groups.[13] The clear presence of an average structure in these crystals creates the impression that the modulations arise from relatively weak interactions that perturb an otherwise established structure.[14] Such is indeed the case in charge density waves.[15-18] In these systems, the wave vectors of the high-energy valence electrons of a system template structural distortions at low temperatures. Likewise, in many other examples, incommensurability can be removed by heating crystals to temperatures at which thermal energy overwhelms the stabilization provided by the modulation.[19,20] It is tempting then to view such effects as low-temperature behavior. In this Article, we illustrate an alternative mechanism in which the atomic framework of the intermetallic material PdBi provides a path for thermal motions to induce rather than suppress modulations.

As with many intermetallic phases,[21-26] the simple nominal composition of PdBi belies a much more complex structural chemistry. A report from Zhuravlev in 1957 noted that PdBi crystallizes in an orthorhombic 2×1×2 superstructure of the TlI-type structure (Figure 1).[27] Later, in 1979, Schubert observed that the compound undergoes a phase transition at 210 °C and that below this temperature the structure exhibits a minute monoclinic distortion (β=89.7°).[28] The origins of the superstructure, the nature of this transition, and the structure of the high-temperature form of PdBi, however, all remain unclear. Without answers to these issues, it is difficult to understand how the structural features of PdBi supports its unique properties, e.g. electrocatalysis for the production of formic acid[29] and non-centrosymmetric superconductivity (T_C = 3.8 K).[30]

Herein, we elucidate the polymorphism of PdBi with a combination of experiment and theory. With variable-temperature single crystal diffraction experiments, we will confirm the general features of PdBi's room temperature 2×1×2 commensurate superstructure (comm-PdBi), and demonstrate that upon heating the superstructure gives way to incommensurate order (incomm-PdBi) with parallels to the recently solved structure of AuIn.[23] In this way, PdBi represents an example of a system in which incommensurability emerges upon increasing rather than decreasing the temperature, joining the brownmillerite-type structures of $Ca_2Al_2O_5$ and

$Ca_2Fe_2O_5$ whose transitions to incommensurately modulated structures occur on heating to 1090 K and 1100 K, respectively.[31,32]

A refinement of the two PdBi structures within the (3+1)D superspace formalism will emphasize the key differences between the commensurate and incommensurate forms of the compound. Through a theoretical analysis, we will see that the form of the comm-PdBi superstructure is encoded in the bonding of the TlI-type parent structure: new Pd-Pd isolobal bonds are needed to reach Pd 18-*n* electron configurations,[33,34] but their formation must navigate steric challenges highlighted by DFT-chemical pressure (CP) analysis.[35-38] However, as the temperature is raised, the CP scheme allows for the dimerization to break down in a gradual fashion, leading to incommensurability. These results illustrate a mechanism for how entropically-driven incommensurability can emerge from frustrated bonding and weakly-coordinated CP networks that can be anticipated with theoretical calculations.

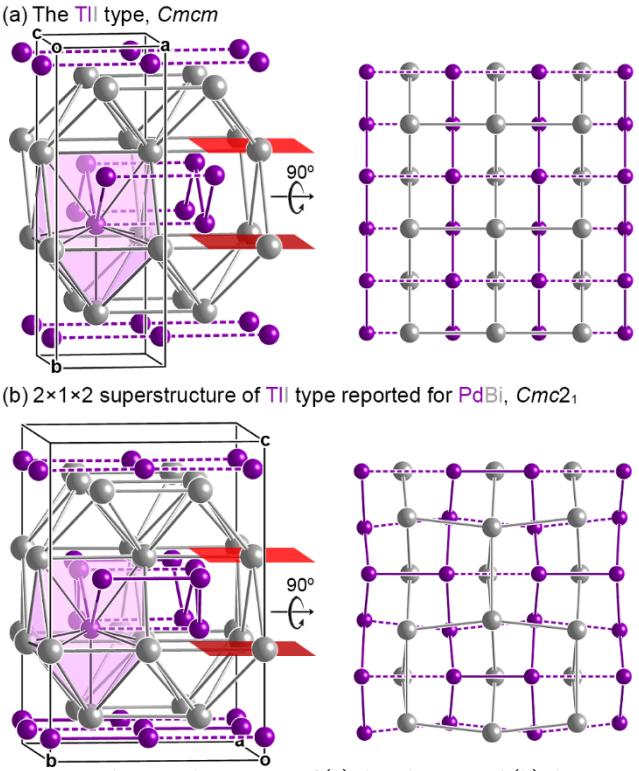

Figure 1. The crystal structures of (a) the TlI type and (b) the 2×1×2 supercell of the TlI type reported for PdBi by Zhuravlev in 1957.[27]

2. EXPERIMENTAL

2.1 Synthesis and Characterization. Crystals of PdBi were grown by sealing equimolar amounts of the pure metals in an evacuated fused silica tube. The sample was subsequently annealed at temperatures suggested by differential scanning calorimetry (see Section 3.1 for further details). First, the sample was heated to 800 °C to form a homogeneous liquid, followed by two annealing steps: crystallization at 350 °C and further treatment at 580 °C to anneal the substucture. This resulted in a silvery metallic ingot that broke into small needle-shaped crystallites when cracked. On an in-house Xcalibur 3 single-crystal X-ray diffractometer, crystals were screened to find a high-quality specimen for further study. That specimen was taken to beamline I19 at the Diamond Light Source, UK, for variable-temperature synchrotron X-ray diffraction. Measurements were taken between room temperature and 300 °C using a hot air stream at a wavelength of λ = 0.4859 Å. To prevent oxidation, the crystal was encapsulated in a quartz capillary. Integration of the data, structure solution, and refinements were carried out with CrysAlisPro,[39] Superflip,[40] and JANA2006,[41] respectively.

2.2 Energy Dispersive X-ray Spectroscopy. To investigate the elemental composition, a PdBi crystal was imaged and analyzed in a Jeol JSM-6700F SEM (voltage 20 keV) equipped with an EDS detector.

2.3 Electronic Structure Calculations. Bonding schemes for both forms of PdBi were calculated with the reversed approximation Molecular Orbital (raMO) method.[42] First, the geometry of each structure was optimized with GGA-DFT,[43,44] using the Vienna Ab initio Simulation Package (VASP).[45-48] Next, single-point calculations were performed on the optimized geometries to obtain band energies and density of states (DOS) distributions to serve as a reference for Hückel models of these compounds. All calculations were performed in the high-precision mode using the projector augmented wave (PAW) potentials[49,50] provided with the package. 10×4×10 and 8×6×5 Γ-centered k-point grids were used for TlI-type PdBi and its commensurate supercell (comm-PdBi), respectively, with an energy cut-off of 313.6 eV.

The program eHtuner[51] was then used to refine the parameters for the Hückel models against the GGA-DFT results. Using these refined parameters, provided in the Supporting Information, simple Hückel calculations were run with the program YAeHMOP[52] on 4×2×4 and 2×2×2 supercells (referring to the conventional cells) of TlI-type PdBi and comm-PdBi, respectively, to ensure that a collection of *k* points in the Brillouin zone of the structures are mapped to the Γ point. The Γ point Hamiltonian was then extracted and imported into the in-house MATLAB programs makeramo, raMOmovie, and Figuretool2 for the raMO analyses.[53]

Using CHGCAR files obtained from the PAW-GGA optimized geometries, band structures for both forms of PdBi were calculated with VASP via non-self-consistent calculations with fixed charge density along specified paths in reciprocal space. For both structures the following path of the monoclinic Brillouin zone was sampled: Γ-A-M-L-V-Z-Γ, with 39 k-points connecting each special point.

2.4 DFT-Chemical Pressure Analysis. The DFT-Chemical Pressure (CP) schemes of PdBi were calculated to assess the role of atomic packing in the structural variations of this system. First, equilibrium ($P = 0$) geometries of each structure were obtained via a geometry optimization step with LDA-DFT using the ABINIT[54-57] software package and Hartwigsen–Goedecker–Hutter norm-conserving pseudopotentials.[58] No significant changes in overall geometry and connectivity, aside from LDA's systematic issue with underestimating cell volumes resulting from the optimizations (see the Supporting Information). Next, single-point calculations were performed at equilibrium volume, as well as slightly contracted and expanded volumes, to produce the kinetic energy and electron densities, as well as the local components of the Kohn-Sham potential used to produce the 3D chemical pressure maps.

From the ABINIT output, CP maps were calculated with *CPpackage2*, using core unwarping with tricubic interpolation[37] as well as the mapping of the nonlocal pseudopotential energies.[38] Then, the CP maps were partitioned into contact volumes between atom pairs using the Hirshfeld-inspired integration scheme.[37] The pressures

within these contact volumes were averaged and projected onto atom-centered spherical harmonics ($l \leq 4$), for visualization with Figuretool2.

To account for charge transfer between Pd and Bi, charged free-ion electron densities were used in the CP analysis during core unwarping and contact volume construction. Atomic charges were extracted from the PAW-GGA electronic structures using the Bader program.[59-62] The Atomic Pseudopotential Engine (APE)[63] was then used to generate radial electron density profiles for a range of percentages of the Bader charge (0% to 75%). The CP results presented in the main text are for 50% of the Bader charges, with the results of the other ionicities presented in the Supporting Information. The results of the CP analyses were found to be qualitatively unaffected by the assignment of reasonable numbers of localized electrons to the Pd for purposes of allocating the Ewald and α energy terms.[38]

3. RESULTS AND DISCUSSION

3.1 Differential Scanning Calorimetry. We began exploring PdBi's polymorphism with differential scanning calorimetry (DSC). On cycling a sample of PdBi between room temperature and 800 °C, three clear features can be seen in the DSC curve (Figure 2). First, two endothermic peaks are found at 583°C and 628°C in the heating curve. On cooling, an exothermic peak arises at 563°C. Two additional features in the heating curve are discernible on closer inspection: a small peak at 210 °C, as previously reported by Schubert,[28] and another at 350 °C.

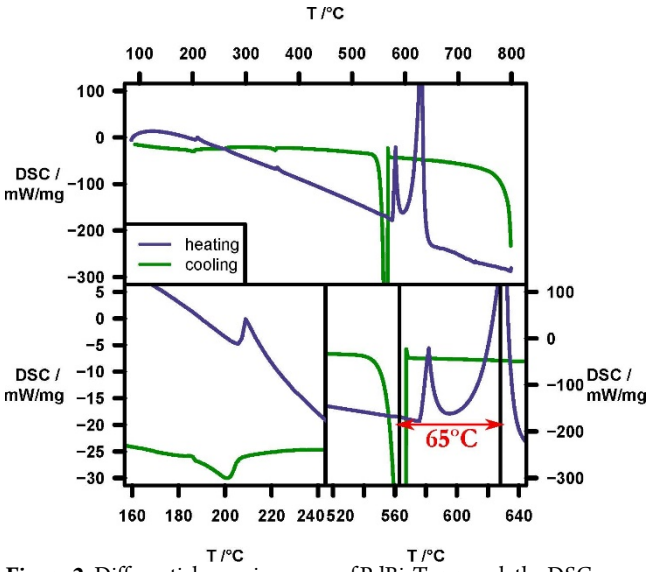

Figure 2. Differential scanning curve of PdBi. Top panel: the DSC curve of PdBi between room temperature and 800 °C. The heating curve is shown in blue, and the cooling curve is in green. Lower left panel: zoomed-in view of the endothermic (blue) and exothermic (green) peaks around 210 °C. Lower right panel: the melting and solidification hysteresis between 520 °C and 640 °C.

The peak at 210 °C coincides with the transition from PdBi rt to PdBi ht described in the phase diagram proposed by Okamoto (Figure 3).[64] The exothermic peaks at 350 °C and 583 °C could denote other processes within PdBi, with the 350 °C feature possibly corresponding to the complete loss of the superstructure to yield a TlI-type structure. They could also reflect the formation or melting of a Bi-poor phase (see phase diagram in Figure 3), respectively. Finally, the endothermic peak at 628 °C can be attributed to the full structure melting (as compared to the phase diagram melting temperature of 618 °C[64]). Following the green, cooling curve (Figure 2), the peak at 563 °C is best attributed to the crystallization of PdBi, 65 °C below where the phase melts in our experiment. Based on these observations, we used the following temperature profile to optimize the growth of PdBi crystals: we first annealed the sample at 350 °C to nucleate PdBi well below its crystallization temperature, then heated the sample to 580 °C (in the middle of the hysteresis range between melting and solidification, Figure 2) to provide the highest possible atomic mobility for the growth of crystals.

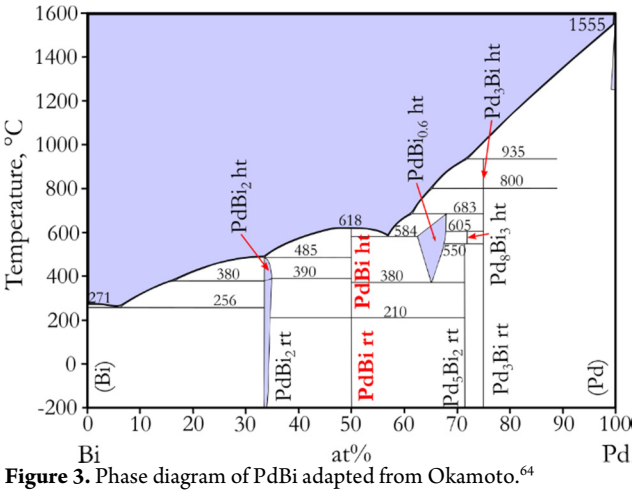

Figure 3. Phase diagram of PdBi adapted from Okamoto.[64]

3.2 Single Crystal X-ray Diffraction of PdBi. With single crystals in hand, we first attempted to understand PdBi's polymorphism via laboratory single crystal X-ray diffraction data. Analysis of the respective data clearly established that the specimen is a single crystal of the PdBi 1:1 phase but shows additional superstructure features. Judging from thermal events observed in the DSC measurement, it seemed likely that uncovering the full details of PdBi's structural chemistry would require X-ray diffraction experiments at various temperatures. To collect data of sufficient intensity and at various temperatures on the small needle-shaped crystallites of PdBi, measurements were conducted at Diamond Light Source's synchrotron beamline I19 between room temperature and 300 °C.

At room temperature, the main reflections in the diffraction pattern of PdBi can be indexed with a unit cell with parameters a = 3.6155(2) Å, b = 10.7047(6) Å, c = 4.3794(3) Å, α = 90°, β = 90.144(5)°, and γ = 90°, corresponding to a TlI-type average cell with a slight monoclinic distortion. These basic cell reflections are joined by satellite reflections at $\mathbf{q}=\frac{1}{2}\mathbf{a}^*+\frac{1}{2}\mathbf{c}^*$, shown in the $hk\frac{1}{2}$ reciprocal lattice layer in Figure 4a. The superstructure reflections fall along the red line along $\mathbf{b}^*$ at a height of $\frac{1}{2}\mathbf{a}^*$ and indicate that at this temperature a 2×1×2 supercell is adopted.

Heating to 200 °C (somewhat below the transition temperature we see in our DSC experiments, though we should note that the temperature here is that at the hot-air nozzle of the heating device rather than the sample) changes the superstructure reflections. The corresponding superstructure reflections are now indexed with $\mathbf{q}$ = 0.4848(6)$\mathbf{a}^*$ + $\frac{1}{2}\mathbf{c}^*$, revealing that PdBi has become incommensurately modulated at this temperature. The small contraction of the satellite reflections causes the peaks in reciprocal space reconstructions to move off the red line, highlighted by red arrows in Figure 4c.

While difficult to discern in the reciprocal lattice reconstructions, the discommensuration is easy to see in histograms of satellite peak counts as a function of distance to the nearest lattice point along **a*** (Figures 4b, 4d).[65]

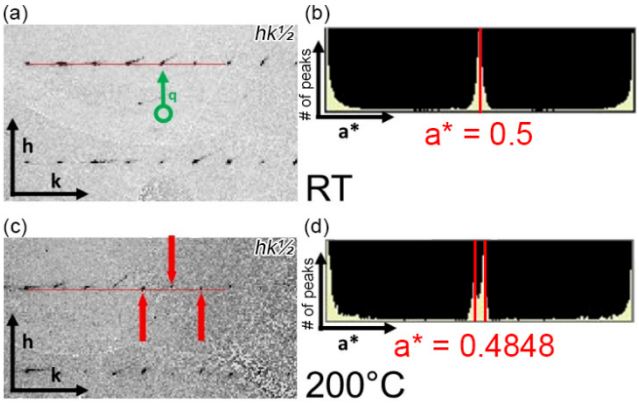

Figure 4. Discommensuration of comm-PdBi upon heating. (a) Reconstruction of the *hk*½ layer of reciprocal space at room temperature. The green circle begins at an absent main peak, with the arrow ending at a satellite. (b) Histogram of peak counts as a function of distance to the nearest reciprocal lattice point along the **a*** direction from CrysAlisPro.[39] (c)-(d) The analogous *hk*½ layer and histogram for PdBi at 200 °C. The red arrows indicate the shortened **q**-vectors. Pairs of satellites from neighboring main reflections are not seen here due to the systematic absence conditions of the superspace group.

We can follow the evolution of the diffraction pattern as PdBi is heated to even higher temperatures, shown in Figure 5 with reconstructions of the *hk*½ reciprocal lattice layer. Figures 5a-b show again the satellite reflections at room temperature and 200 °C, respectively. In comparing these two images, the split from **q** = (½, 0, ½) to **q** = (0.4848(6), 0, ½) is once again indicated by the slight perturbation of the satellite peaks when traveling along **a***. Heating to 220 °C (Figure 5c) leads to a small contraction of the **q**-vector to (0.4823(9), 0, ½), but also to the evolution of diffuse scattering under the positions of the satellite reflections. At higher temperatures the **q**-vector begins to lengthen, although the numbers become less reliable due to the upsurge of diffuse scattering. By 250 °C (Figure 5d), the satellites have essentially vanished and the diffuse scattering begins to dominate the reciprocal lattice reconstruction. Above this temperature, the diffuse scattering grows so weak that it is barely visible, suggesting that PdBi has essentially transformed to the TlI-type parent structure.

Throughout this process, the satellite reflections show variability in their positions along the **a*** axis, but their component along **c*** stays fixed at ½**c***. To model these features, it then becomes convenient to treat the **c*** component of the satellites by doubling the cell's *c*-axis and to handle the **a*** component as a modulation using (3+1)D superspace techniques. This procedure yields non-standard settings for the two modifications and unusual expressions for the equivalent positions, but it makes them directly comparable, having metrically the same unit cell (up to a small deviation in the monoclinic angle). As we will see below, this would not be possible using the **q**-vector (½, 0, ½) since it is compatible with a unique *b*-axis but not a unique *a*-axis.

In this way, comm-PdBi is described as a commensurately modulated monoclinic structure whose basic cell has a doubled *c*-axis when compared to the TlI type, with unit cell parameters a = 3.6155(2) Å, b = 10.7047(6) Å, c = 8.7588(6) Å, α = 90°, β = 90.144(5)°, γ = 90°, and **q** = (½, 0, 0). Likewise, incomm-PdBi is indexed with a similar unit cell: a = 3.625(2) Å, b = 10.6736(6) Å, c = 8.8428(5) Å, β = 89.966(5)°, and a modulation vector of **q** = (0.4848(6), 0, 0).

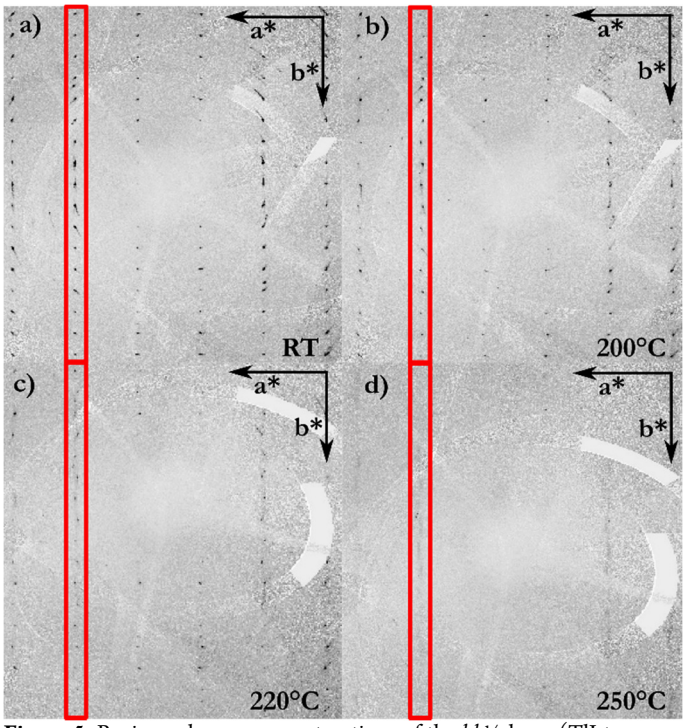

Figure 5. Reciprocal space reconstructions of the *hk*½ layer (TlI-type setting) at (a) RT, (b) 200 °C, (c) 220 °C, (d) and 250 °C.

3.3 Refinement of the Crystallographic Models.

To begin solving the structures of PdBi at room temperature and 200 °C, we first need to assign the correct space group, which proved to be non-trivial in this case. This fact is underscored by the previous reports on the structure, where the space groups $Cmc2_1$[27] and $P2_1$[28] have both been cited as solutions. The lattice parameters observed here are nearly metrically orthorhombic but attempts to solve and refine the structure indicated that lowering the symmetry to monoclinic is necessary. In the case of the room temperature structure, trial and error indicates that the *b*-axis should be taken as unique.

The symmetry reduction from orthorhombic to monoclinic (unique *b*) lowers the space group from *Cmcm* to its *C* 1 2/*c* 1 subgroup. With **q** = ½, 0, ½ (the standard setting), this would have yielded the (3+1)D superspace group *C* 1 2/*c* 1(*a*0*γ*). By instead doubling *c* and setting the **c*** component of **q** to 0 we arrive at a non-standard setting of the same superspace group with an *X*-centering. Here, *X* refers to the centering vectors (0, 0, ½, ½), (½, ½, 0, 0), and (½, ½, ½, ½), as suggested by the systematic absence conditions *hklm*: $l+m = 2n$, $h+k = 2n$, $h+k+l+m = 2n$. The general positions for the superspace group in this setting are (x_1, x_2, x_3, x_4), (-x_1, x_2, ¼-x_3, ¾-x_4), (-x_1, -x_2, -x_3, -x_4), and (x_1, -x_2, ¼+x_3, ¾-x_4). A more detailed derivation of the (3+1)D superspace group can be found in Section S2 of the Supporting Information.

Of the numerous alternatives we tried, structure solution and refinement in this space group provided the best agreement factors (Table 1). Here the orthorhombic pseudosymmetry is reflected in

imbalanced twinning, with individual 1 having a much larger volume of 87% than individual 2 with 13%.

The atomic model for comm-PdBi's structure uses one symmetry distinct site for the Pd atom and one symmetry distinct site for the Bi atom. In this model, the Pd atoms are split into pairs of distinct but symmetry-related domains along the x_4 axis, modeled with one crenel wave, as well as a sinusoidal wave to give a small amount of curvature (Figure 6a). The domains are centered at different x_1 positions (red and magenta) on either side of the green dashed line, which indicates the glide operation transforming the magenta into the red position and vice versa. This corresponds to Pd atoms displaced along $+x_1$ or $-x_1$. The Bi site meanwhile is described with first and second order harmonic waves (Figure 6b) which represent motions that are coordinated with the Pd displacements, as we will examine more closely soon.

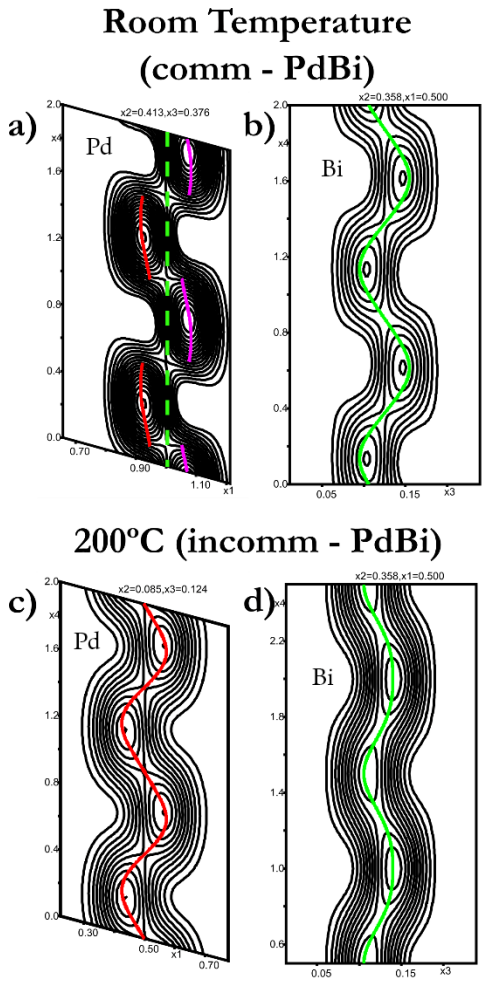

Figure 6. (3+1D) models of comm- and incomm-PdBi. (a) Cross-section of the Fourier electron density associated with the Pd site in the room temperature refinement of PdBi. Two symmetry-related atomic domains for Pd are shown in red and magenta, with the glide operation relating the two positions shown in green. (b) Cross-section for the Bi atom at room temperature with the green line showing its atomic position. (c)-(d) Corresponding plots for the 200°C data set, with red and green lines indicating the models' Pd and Bi positions, respectively. As the slices are not integrated over any thickness along the other directions, the electron density values should be viewed qualitatively.

The atomic geometry of comm-PdBi's structural model is shown in Figure 7. Here, the Pd atoms distort away from the Tl positions of the TlI-type average cell (Figure 7a) to create pairs along the *a*-axis, encoded by the crenel functions' alternation along *x*. Moreover, the phase of the pairing changes as one moves along the *c*-axis to create a sequence of Pd_2 pairs (S) and Pd···Pd gaps (L) in an …SSLLSSLL… pattern. In this way, an alternation of rectangles and flattened octagons, which we might refer to as an 8484 pattern, appears when moving along the *a*-axis (as in Figure 7b). This doubles the repeat period of the structure along *c* relative to that on the original TlI-type cell, accounting for the ½**c*** component to the **q**-vector.

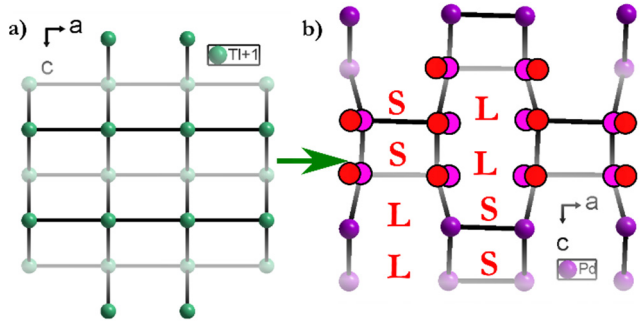

Figure 7. Pd connectivity in (a) TlI[67] and (b) comm-PdBi. The red and magenta circles refer to the modeled atomic domains shown in Figure 6.

Table 1. Crystallographic information for the PdBi polymorphs.

Temperature	RT	200°C
Refined formula	PdBi	
Formula weight, M_r	315.4	
Crystal size (mm^3)	0.05 × 0.4 × 0.05	
Color	Gray	
Crystal system	Monoclinic	
Space group	$X12/m1(a00)00$	$X2/m11(a00)00$
Lattice parameters	$a = 3.6155(2)$	$a = 3.625(2)$
	$b = 10.7047(6)$	$b = 10.6736(6)$
	$c = 8.7588(6)$	$c = 8.8428(5)$
	$\beta = 90.144(5)$	$\alpha = 89.966(5)$
Modulation vector	(0.5, 0, 0)	(0.4848(6), 0, 0)
Maximum order of satellites	1	1
Formula units	8	8
Refinement Method	F^2	
R_{int} ($I > 3\sigma$)	9.37	7.95
R_{obs} ($I > 3\sigma$, *all*)	8.54, 9.08	6.99, 8.04
wR ($I > 3\sigma$, *all*)	25.36, 27.82	18.67, 19.44
R_{main} ($I > 3\sigma$)	5.61	6.66
R_{sat} ($I > 3\sigma$)	10.43	7.26
GOF ($I > 3\sigma$, *all*)	1.85, 1.90	1.96, 2.15
No of parameters	28	25
CCDC No.	1900572	1900573

At first, we modeled the high temperature data with an analogous model, only changing the **q**-vector from (0.5, 0, 0) to (0.4848(6), 0, 0). For this polymorph, however, changing the setting so that *a* is now the unique axis with a monoclinic angle $\alpha = 89.966(5)°$ results in a far superior solution. The (3+1)D superspace group becomes $X2/m11(\alpha00)00$.[66] Another change in the high temperature model is the treatment of the Pd atoms: the two distinct Pd domains merge

into a more continuous function, which can be modelled with two sinusoidal waves (just like the Bi positions, see Figures 6b,d).

Despite the change in the orientation of the unique axis, the placement of atoms and their networks are remarkably similar in the comm- and incomm-PdBi models, at least at the local level. At 200 °C, the incommensurate modulation leads to changes at a longer length scale: comm-PdBi's pattern of Pd-Pd pairing is interrupted by stacking fault-like slabs where the dimerization is lost. This insertion of faults is illustrated for a section of the structure (generated at $t_0 = 0$) in Figure 8. We begin on the left with a connection fault, where the structure displays an essentially undistorted TlI-type network. Further along the *a*-axis, the Pd-Pd interatomic distances gradually lengthen and shorten to bring back the 8484-type network we see in comm-PdBi. Closing in on the next fault, the interatomic distances even out again until they reach their original TlI-type pattern.

Because a supercell's size along a crystallographic direction is the reciprocal of the **q**-vector's length, the frequency of these stacking faults can be simply related to the change in the **q**-vector upon heating. Going from room temperature to 200°C leads to a shift of **q** from (0.5, 0, 0) to (0.4848(6), 0, 0), which corresponds to a disruption of the comm-PdBi structure in the high temperature incomm-PdBi phase at a spacing approximated by the expression,

$$\frac{1}{q_{\alpha,RT} - q_{\alpha,200\,°C}} = \frac{1}{0.5 - 0.4848} \approx 66.$$

The number of atoms between the centers of the faults shown here is in fact 33, *i.e.* half the number of the atoms predicted for the superstructure.

This structural sequence suggests an interesting balance of energetics and entropy are at work in this compound. At low temperatures, the Pd-Pd pairing follows a commensurate pattern with no connectivity faults appearing in our model. These findings are a hint that this is the lowest energy configuration. The introduction of these faults as the temperature is increased indicates that the incommensurability is entropically stabilized. These trends are consistent with a lock-in behavior on reducing the temperature, with the structure going from modulated to non-modulated. In the next section, we will see how this behavior is in fact encoded in the atomic packing and electronics of this compound, using simple bonding schemes and a chemical pressure analysis.

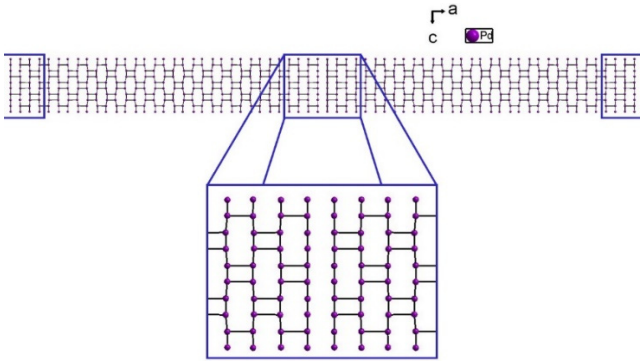

Figure 8. Connection faults in incomm-PdBi at 200°C. The number of atoms separating the leftmost and central fault is 33; the central and rightmost faults are separated by 34 atoms.

3.4. Electronic Driving Force for the Formation of comm-PdBi. Now that we have a model for the structural variations that PdBi undergoes as a function of temperature, let's examine the chemical factors driving this progression. We begin by considering the advantages conferred by the room temperature superstructure of comm-PdBi over its simpler TlI-type parent structure. The most striking difference between these two forms is in their Pd-Pd connectivity. In the TlI-type parent structure, the Pd atoms form a zigzag chain running along *c* with Pd-Pd distances of 2.88 Å. These chains are relatively isolated from each other, with the shortest inter-chain distances (3.68 Å) arising as the chains stack along *a*. In the transition to comm-PdBi, Pd zigzag chains twist to create pairings in the inter-chain Pd-Pd contacts; the regular spacing along *a* in the TlI-type gives way to an alternation of short (3.09 Å) and long (4.22 Å) distances in comm-PdBi. The former contacts are now short enough for Pd-Pd interactions to become non-negligible.

Structural distortions of this type are highly suggestive of a process driven by states at the Fermi surface, such as a Peierls transition[68] or charge density wave.[69] A hallmark of such phenomena is the appearance of a band gap or pseudogap in the electronic band structure at the Fermi energy (E_F), which can be detected as a minimum in the density of states (DOS) distribution. In Figure 9, we compare the DOS curves calculated for TlI-type and comm-PdBi. Both exhibit a set of Bi s states at ca. -16 to -18 eV, as well as a large block of Pd d states right below the E_F, with the higher energy states being largely based on the Bi p, Pd s, and Pd p orbitals.

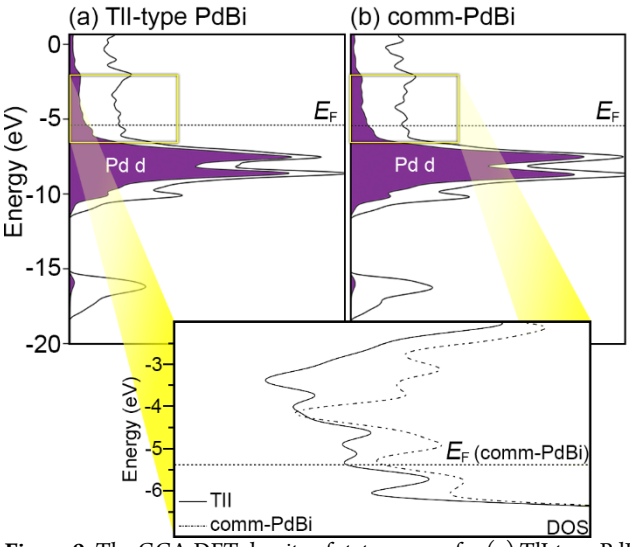

Figure 9. The GGA-DFT density of states curves for (a) TlI-type PdBi and (b) comm-PdBi. The features near the E_F are overlaid in the inset.

Curiously, these similarities extend to the region near the E_F. No clear pseudogap arises in the transition to comm-PdBi. Zooming in on this energy range reveals only slight differences: each structure places the E_F in a shallow local minimum in the DOS. While this minimum at first seems more distinct for the case of comm-PdBi, the absolute value of the DOS (scaled to the same number of formula units) is larger here than for the TlI type. A close look at the band dispersions between special points in the Brillouin zone leads to the same conclusion (see the Supporting Information). The opening of bands around the E_F is evident at one special point, but there is the closing of bands at others (Figure S3). Taken together, the formation of comm-PdBi does not appear to be chiefly driven by electronic states near the E_F.

An alternative hypothesis that is less focused on the region near the E_F is provided by the 18–*n* rule,[34] in which the structural preferences of the Pd atoms are assumed to be guided by the favorability of 18-electron configurations, such that all their valence s, p, and d orbitals are utilized. In this bonding scheme, transition metal (T) atoms can share electron pairs with each other in multi-center, main-group atom-supported functions isolobal to traditional T-T bonds. Through electron sharing, the T atom can reach an 18-electron configuration with only 18–*n* electrons, where *n* is the number of T-T isolobal bonds in which it participates.[34]

From this point of view, a driving force for the distortion becomes clear. As PdBi has 10 + 5 = 15 valence electrons/Pd atom, each Pd would need to engage in three Pd-Pd bonds to reach an 18-electron configuration. In the original TlI-type structure, the contacts along the Pd zigzag chains would allow for two such bonds. However, in the absence of π interactions, each Pd atom would still be 1 electron short of the 18–*n* count. On the other hand, the formation of the comm-PdBi superstructure allows each Pd atom to make one additional Pd-Pd contact, suggesting that the distortion serves to counteract this electron deficiency, with the effects being distributed among the occupied crystal orbitals rather than focused on the states near the E_F.

The reversed approximation Molecular Orbital (raMO) method[42] offers an approach to explore this notion. In this method, the occupied crystal orbitals from a DFT-calibrated Hückel model of the compounds are used as a basis set to reproduce local Molecular Orbital diagrams. The results of the analysis are a set of raMO functions that represent the best possible reconstructions of the target MOs from linear combinations of the occupied orbitals.

To examine the role of 18-electron configurations, we started with the raMO reconstruction of a Pd atom's s, p and d valence orbitals in the two structures (see the Supporting Information). After seeing that the Pd 4d raMOs are tightly localized (corresponding to closed d^{10} subshells), we focused on the raMOs generated for the 5s and 5p orbitals. These reveal electron-sharing between Pd atoms, which is easiest to see after taking linear combinations to create hybrid functions (Figure 10).

For TlI-type PdBi (Figure 10a), the trigonal planar Pd environment suggests sp^2 hybridization, which we obtain via linear combinations of the 5s, $5p_x$, and $5p_y$ raMOs. Two of these show Pd-Pd bonding character, sharing the same nodal properties as a typical σ bond but are supported by the surrounding Bi coordination sphere; these are the two isolobal Pd-Pd bonds along the chain that we anticipated above. The third sp^2 hybrid resembles a Pd lone pair that engages in bonding with the surrounding Bi atoms. The raMO for the unhybridized $5p_x$ orbital partakes in π interactions along the Pd zigzag chain, reflecting the electron-poor character of the phase.

In the transition to comm-PdBi with the new Pd-Pd contacts, the 5s and 5p raMOs can now be combined in an sp^3 fashion to create three isolobal bonds and a lone pair (Figure 10b). This presence of three Pd-Pd bonds is just what the Pd needed to achieve its 18-electron configuration. However, hints of Pd-Pd π interactions remain along the zigzag chain, suggesting that the Pd atoms still have some electron deficiency. Apparently not all of the 15 electrons/Pd atoms in the structure are associated with the Pd centers.

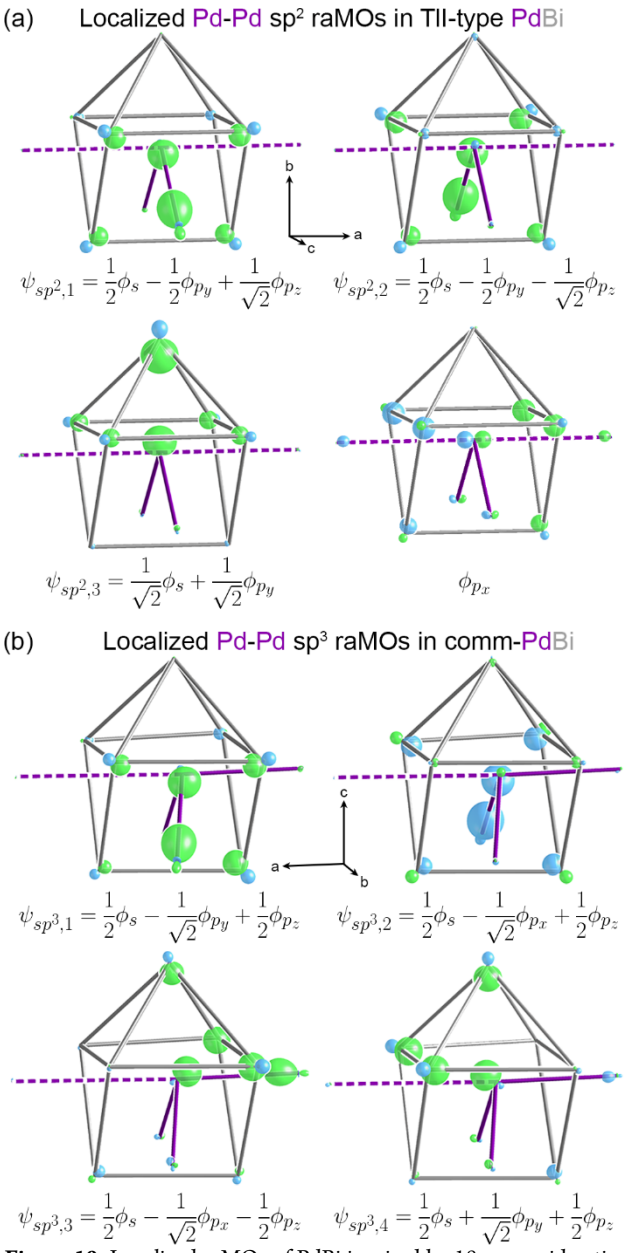

Figure 10. Localized raMOs of PdBi inspired by 18–*n* considerations. (a) In TlI-type PdBi, the TlI-type PdBi forms sp^2 bonding interactions along the zigzag chains, as well as a lone pair function. The unhybridized $5p_x$ raMO shows π interactions, indicating that the phase is electron poor. (b) In comm-PdBi, a third Pd-Pd bonding contact is formed, resulting in sp^3 hybrid functions. π interactions remain along the zigzag chain (signaling electron deficiency).

Where are the remaining electrons? To isolate these electrons, we attempt to create raMOs for each of the 128 Pd atoms in a 4 × 2 × 4 and 2 × 2 × 2 supercell of TlI-type PdBi and comm-PdBi, respectively. The results of such an analysis on TlI-type PdBi are shown in Figure 11. The Pd 4d orbitals again give rise to tightly localized functions, shown as the filled-in portion of the DOS in Figure 11a. The remainder states left over from these reconstructions then serve as the basis set for construction of, first, two sp^2 bonds and, then, one sp^2 lone pair on each Pd atom, a process called a remainder analysis.[70,71] We can successfully reproduce 117/128 possible Pd-Pd bonding functions along the zigzag chain in TlI-type PdBi, corresponding to 1.82 electrons/formula unit being localized to these

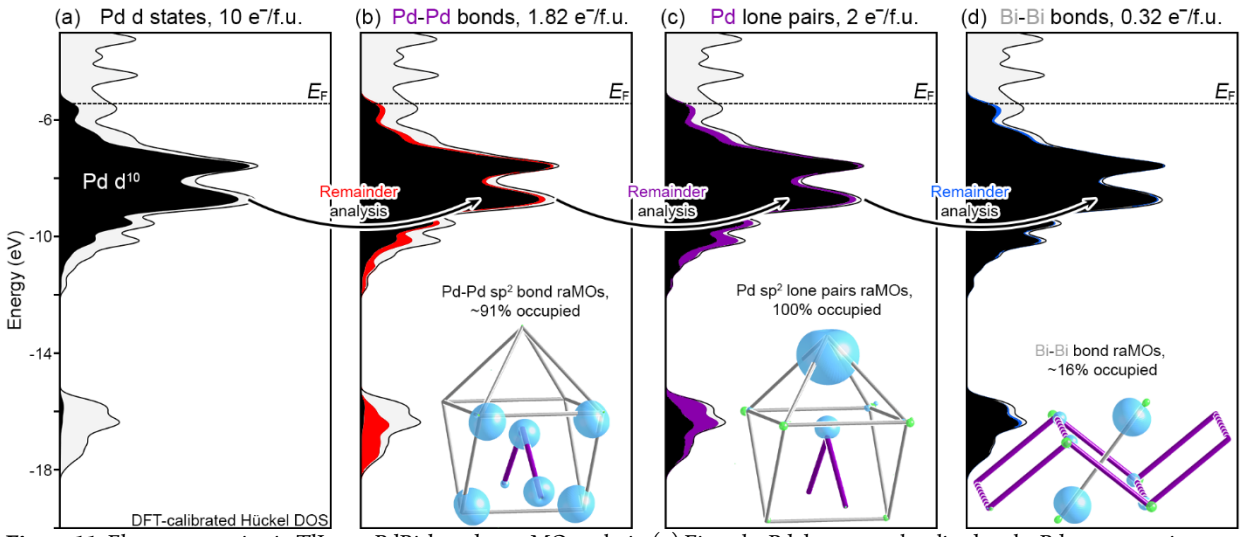

Figure 11. Electron counting in TlI-type PdBi, based on raMO analysis. (a) First, the Pd d states are localized to the Pd atoms, serving as a closed shell. Then, subsequent remainder analyses reveal (b) 1.82 e^-/f.u. localized to Pd-Pd sp^2 bonding functions, (c) 2 e^-/f.u. in sp^2 lone pairs, and (d) small occupation of a bonding function associated with a Bi-Bi bridging contact.

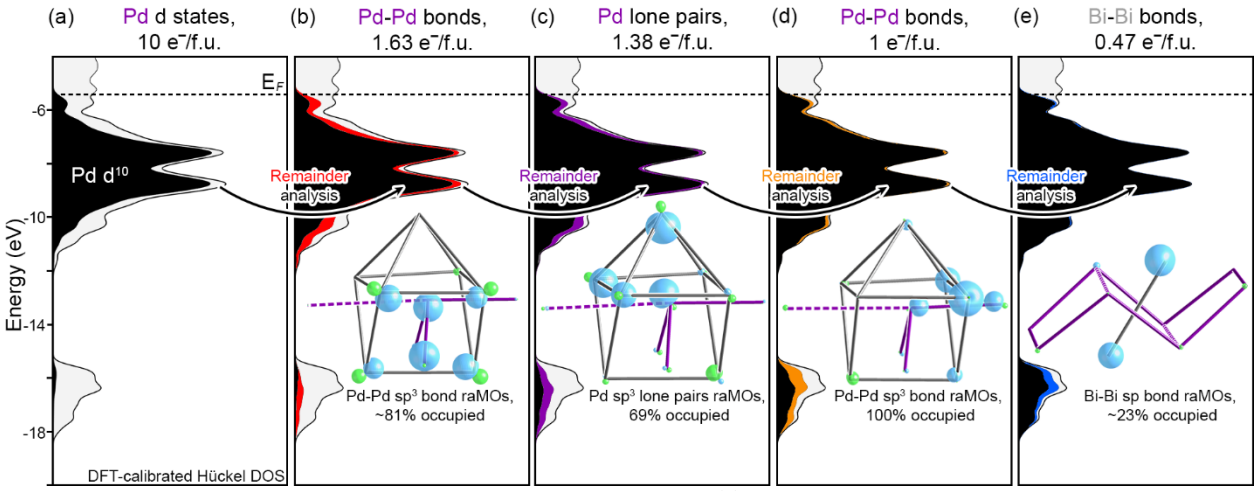

Figure 12. Electron counting of comm-PdBi, as derived from raMO analysis. (a) The Pd 4d orbitals compose a closed shell. Attempts to reproduce three Pd-Pd bonds and a Pd lone pair reveal (b) partial occupation of the zigzag bonding functions and (c) the Pd lone pairs, as well as (d) full occupation of the new Pd-Pd bonds connecting adjacent zigzag chains. (e) A portion of the remaining electrons is in the Bi-Bi bonding function bridging non-bonding Pd atoms in different zigzag chains, with the rest occupying delocalized Bi states.

functions (Figure 11b). A second remainder analysis successfully reconstructs all 128 sp^2 lone pairs (Figure 11c), accounting for another 2 electrons/formula unit.

At this point, 13.82 of the 15 electrons per formula unit are accounted for. A likely place to search for the remaining electrons is in the unhybridized Pd p_x orbital. These reconstructions, however, quickly lead to delocalized Bi-rich states. In turning our attention then to the Bi sublattice, we can localize ~0.32 of the remaining electrons to a Bi-Bi bonding function that bridges the zigzag chains of the structure (Figure 11d). The remaining 0.86 electrons/formula unit are more diffusely spread across the structure. Clearly, this is not an ideal bonding situation.

An analogous treatment of comm-PdBi reveals substantial improvement in the electronic situation (Figure 12). Here, the Pd atoms still retain closed-shell 4d configurations (Figure 12a). In the next steps of the raMO analysis, we try to reconstruct the sp^3 functions mentioned above: three Pd-Pd bonds and one lone pair. First, the attempt to reconstruct isolobal bonds along the zigzag chains uncovers considerable occupation of these bonding functions, with 104 of the 128 possible zigzag bonds successfully reproduced (Figure 12b).

Next, the remaining electrons serve as a basis for the reproduction of an isolobal bond along the newly contracted Pd-Pd contact along *a*, as well as Pd sp^3 lone pairs in the resultant long Pd-Pd contacts along *a*. Reconstructions of the lone pairs reveal 88/128 occupied states (Figure 12c), which is in fact a decrease from the case of the original TlI structure. The Pd-Pd isolobal bonds at the shortened contacts along **a**, however, are very well recreated, with all 64 states being occupied (Figure 12d). A final remainder analysis reveals slightly more occupation of the bridging Bi-Bi bonding function, with just shy of 0.5 electrons/formula unit existing in these functions. In total, 14.48 electrons/formula unit are localized through this analysis, with the unlocalized DOS corresponding to delocalized Bi-based states (Figure 12e). While there is still substantial metallic

character in the bonding of comm-PdBi, it exhibits a much higher degree of localization than its TlI-type parent structure.

Overall, the comparison of the raMOs of TlI-type comm-PdBi suggests that the creation of new Pd-Pd bonds provides an energetic driving force for the formation of the superstructure. The full optimization of the bonding is limited, however, by competing electronic states, particularly the presence of low-lying Bi-Bi bonding functions along contacts that are isolated from the Pd atoms. The result is a curious juxtaposition of a structure that follows the geometrical prescriptions of the 18–*n* rule without a significant pseudogap appearing at the E_F.

3.5. Atomic Packing Consequences for Atomic Motion in PdBi. The non-ideal bonding in the comm-PdBi superstructure would seem to set the stage for a transition to the TlI-type parent structure at higher temperatures. Experimentally, though, this is not the first thing that is observed upon heating. Instead, an incommensurate structure containing strip-like domains of the TlI-type appears. What underlies the formation of this intermediate step? One promising way to find answers is by investigating how the atomic packing factor directs atomic motions during these phase transitions. The DFT-Chemical Pressure (CP) method provides a way to visualize such effects. With this method, the macroscopic internal pressures of a phase, as obtained in a DFT calculation, are resolved into competing interatomic pressures that call for either the expansion or contraction of different portions of the structure. The resulting schemes can highlight frustration in the space requirements of the atoms as well as potential paths of facile motion.

In Figure 13, we show the CP scheme calculated for TlI-type PdBi, focusing on the capped trigonal prismatic coordination environments of the Pd atoms. The scheme is represented with atom-centered radial plots, where the size of the lobes is proportional to the magnitude of the sums of the pressure contributions experienced by an atom along that direction, while the colors of the lobes indicate their signs. Black lobes represent negative pressures, or contacts that would prefer contraction of the structure, while white lobes represent positive pressures, or contacts that would benefit from the expansion of the structure.

In TlI-type PdBi (Figure 13), each Pd atom experiences an asymmetric distribution of positive CP; the largest lobe is along the apical Pd-Bi contact of 2.87 Å, while four smaller lobes radiate towards equidistant basal Pd-Bi contacts of 2.90 Å. The Bi CP distributions also reflect these positive CPs along Pd-Bi contacts with white lobes directed toward the Pd atoms. The Bi atoms also show the counterforce that prevents the structure from simply expanding in response to the overly short Pd-Bi contacts: large negative lobes pointing along Bi-Bi contacts. Relieving the positive pressures within the Pd-Bi interactions through expansion of the structure would require unfavorable stretching of the Bi sublattice.

Together, these features guide how atoms can move from the TlI-type parent structure to form comm-PdBi. The motions of the Pd atoms along *a* to form new Pd-Pd interactions increase the distance of the apical Pd-Bi contact. This releases the major positive CP feature in the parent structure—every Pd atom would be expected to take advantage of this. At the same time, though, the formation of new Pd-Pd bonds should avoid compressing the already too-short Pd-Bi contacts and stretching the Bi-Bi ones.

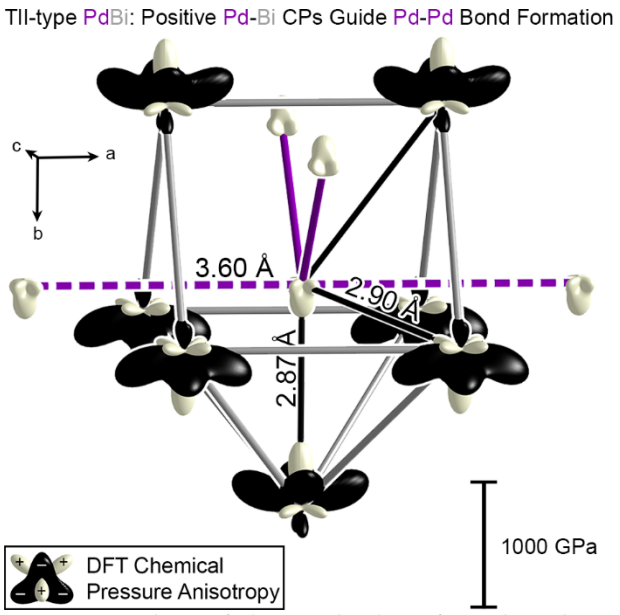

Figure 13. CP scheme of TlI-type PdBi shown for a Pd coordination environment. The Pd-Bi CPs are positive, while the Bi-Bi CPs are negative.

In Figure 14, we focus on how these factors play out in the formation of the comm-PdBi structure. We begin by considering a single Pd/Bi layer in TlI-type PdBi running perpendicular to the *b*-axis (Figure 14a). Here, the same CP features are evident: positive Pd-Bi CPs (highlighted with red lines) and negative Bi-Bi CPs (black dotted lines). Figure 14b shows the corresponding slab in the comm-PdBi structure, with the yellow arrows highlighting the atomic motions that have taken place. A pairing of two Pd atoms necessitates the bridging Bi atoms in the same layer to move away from the nascent bond. The displaced Bi atoms in turn push apart the neighboring Pd-Pd pairs along the *c*-direction, leading to the pairing in the next Pd chain running along *a* to be out-of-phase. The continued propagation of this pattern leads to an alternation of Pd-Pd pairs and gaps in a checkerboard pattern. Stacking the two layers of the slab results in the 8484 pattern of Pd-Pd contacts mentioned in Section 3.3 (Figure 14c). In this way, the structure of comm-PdBi is essentially determined by the desire of each Pd atom for one additional close Pd-Pd contact and the pattern of Pd-Bi positive CPs.

The 2×1×2 superstructure of the TlI-type exhibited by the comm-PdBi structure would thus seem to represent the ground state of the system from both the electronic and atomic packing viewpoints. How, then, does the incommensurate structure emerge as the temperature of the system is increased? To understand this, it is useful to consider the CP issues that would arise from a local breakdown of the Pd_2 dimer pattern along the *a*-axis in comm-PdBi. In Figure 15, we use a layer of the TlI type to show how the insertion of an unpaired Pd atom, which we will call a monomer (red circles), can be accommodated.

On both sides of the monomer, the formation of the neighboring dimers would set off a pattern of atomic motions to accommodate the Pd-Bi positive CPs (as we saw for the formation of comm-PdBi). This time, however, the presence of the monomer means that some of the Bi displacements induced by the positive CPs on the neighboring Pd_2 dimers interrupts the pairing pattern along *a* for Pd atoms in the chains above and below the central one, as marked with x's in Figure 15. The result: the presence of one monomer promotes the

propagation of a larger pattern of monomers across the *ac*-layer (dashed red circles in Figure 15a).

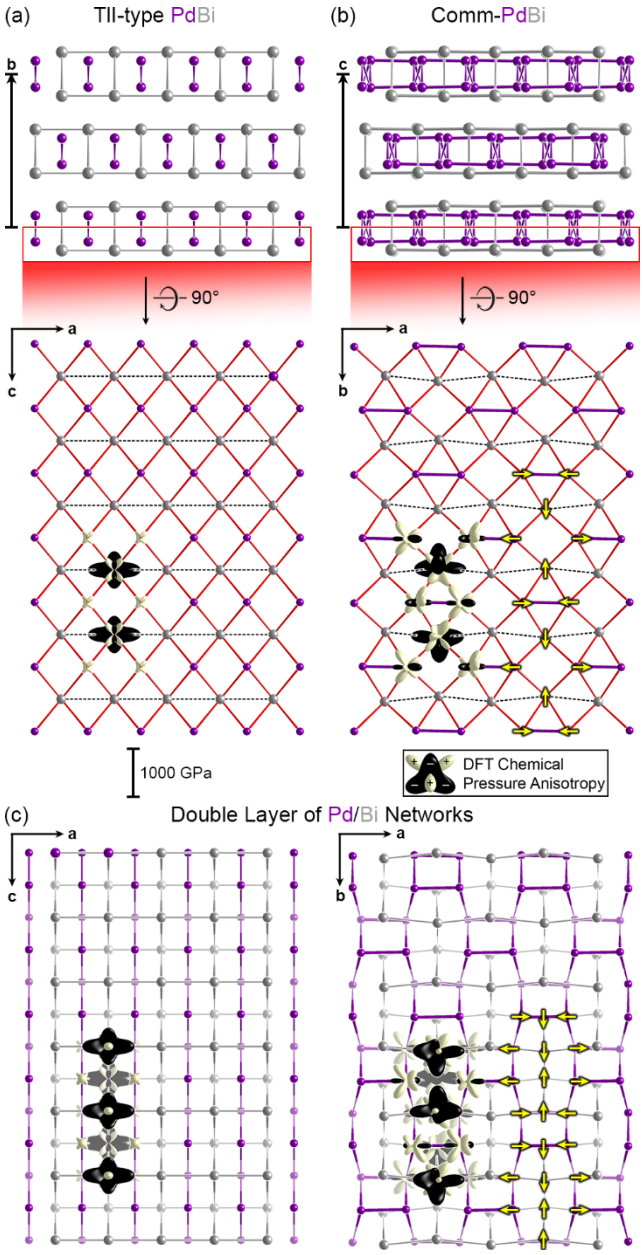

Figure 14. The CP tensions within a single layer of TlI-type and comm-PdBi. In both structures, Pd-Bi bilayers are stacked along the long axis. Viewing a single layer of the PdBi structure highlights the CP tensions: positive Pd-Bi CPs (connected by red lines) and negative Bi-Bi CPs (black dotted lines). Transitioning from (a) TlI-type PdBi to (b) comm-PdBi, results in Pd-Pd bonds along *a* that distorts the Pd sublattice. Pd-Bi positive CPs within the layer necessitate the alternation of Pd dimers; the resulting motions are highlighted with yellow arrows. (c) Stacked Pd-Bi layers in TlI-type PdBi (left) and comm-PdBi (right). The resulting 8484 pattern of comm-PdBi can be derived from the CP tensions of the parent structure.

From a central monomer, there are several possible paths for the monomers to spread. The new monomers might occur either on opposite sides along *a* of the initial one (a *trans* arrangement, Figure 15a), or on the same side (a *cis* arrangement, Figure 15b). That these two patterns are not equally favorable can be seen from a close examination of the atomic packing requirements around the initial monomer. In the *trans* arrangement, the Pd-Bi displacements rippling around the initial monomer lead to it being compressed by Bi atoms on opposite sides. As the Pd-Bi atoms are already overly short in the TlI-type parent structure, this would be expected to introduce extra tension in the structure's atomic packing.

The situation is different for the *cis* arrangement. Again, the two concerted atomic motions lead to two Bi atoms coming closer to the Pd monomer. Now, though, they approach the monomer from the same side, leaving open a path for it to move away in the opposite direction toward a neighboring Pd dimer, even offering the potential for the formation of a Pd trimer. In this way, the *cis* arrangement allows for the interruption of the Pd-Pd pairing pattern of comm-Pd without obvious exacerbation of the structure's CP issues relative to the parent structure. At least in terms of atomic packing, this appears to be the more favorable arrangement.

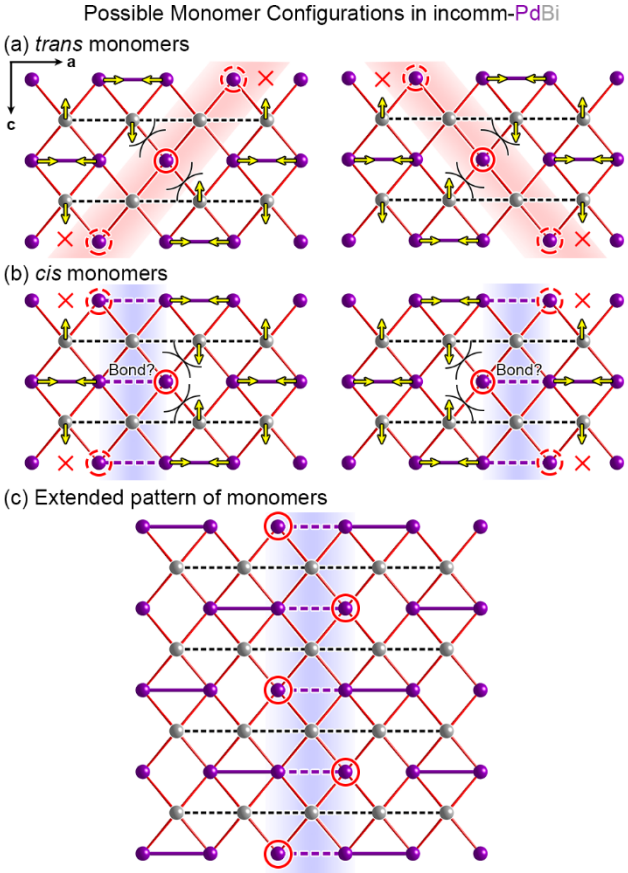

Figure 15. The possible configurations of disrupted Pd-Pd dimers in incomm-PdBi. (a) Monomers arranged *trans* to each other (red circles). These arrangements leave a Pd atom with shortened Pd-Bi contacts. (b) A *cis* arrangement for the monomers, where the monomers are given the flexibility to move and possibly form Pd trimers. (c) The extended pattern of monomers in a *cis* arrangement, which closely matches the observed connection faults in the incomm-PdBi structure.

What about the electronic consequences of disrupting the Pd-Pd pairing? According to the 18–*n* rule, each Pd atom seeks to gain one additional isolobal Pd-Pd bond when distorting away from the TlI type. In the comm-PdBi structure this is accommodated by a strict dimerization pattern. Monomers, of course, will not have any addi-

tional Pd-Pd interactions relative to the TlI type, and so their incorporation would lead to the phase becoming increasingly electron poor. For the *trans* monomer arrangement where the Pd monomers are squeezed from opposite sides, this would be the end of the story. With the *cis* arrangement, on the other hand, the monomer has the option of joining a dimer to form a trimer, where one Pd atom has two rather than one extra Pd-Pd interaction. Through a balancing of trimers and monomers–in a likely dynamic way at high temperatures–the correct average number of new Pd-Pd contacts can be maintained.

This viewpoint accounts for the overall features of the incommensurate structure of PdBi at 200°C, as it was depicted in Figure 8. The incommensurability results from the insertion of connection faults running along *c* into the comm-PdBi structure. The Pd-Pd patterns within these faults appear on average like domains of the TlI-type. A close inspection of the central regions for a column of Pd monomers, however, reveals a *cis* arrangement. In fact, the alignment of the incommensurate component of the **q**-vector with the *a*-axis can be seen as a direct consequence of the preference for the *cis*- over the *trans*- configurations of adjacent monomers.

Viewed together, the results of our analyses of comm- and incomm-PdBi reveal the factors governing their relative stabilities. The comm-PdBi structure allows for the release of the major Pd-Bi positive pressure (the apical Pd-Bi contact in the Pd coordination environment) while achieving a Pd-Pd connectivity in accord with the 18–*n* rule, all without going significantly against any of the other positive CPs in the structure. The incorporation of Pd monomers in the incommensurate structure introduces more ambiguity in the Pd-Pd connectivity and will partially undo some of the CP relief along the apical Pd-Bi contacts. The energetic penalties here would seem to make the incommensurate structure unfavorable at low temperatures, where entropic effects will be marginal.

At higher temperatures, though, the greater entropy provided by geometrical flexibility of the incommensurate structure would likely enhance its thermodynamic stability relative to the comm-PdBi phase. We previously discussed how the incommensurate structure could offer interchanges of monomers and trimers. In addition, the CP scheme of TlI-type PdBi suggests that the connectivity faults could be regions with soft atomic vibrations that could enhance the entropy (Figure 12). Note that the CP features of the Bi atoms in this parent structure show strong positive pressures perpendicular to negative pressures, giving rise to quadrupolar character that has been associated with soft atomic motions.[72] As this quadrupolar nature is less prominent in the CP scheme of comm-PdBi structure, the reversion to the TlI-type structure in the connectivity faults offers new vibrational freedom. Overall, then, PdBi represents a case in which incommensurability occurs from the CP-guided path to incorporating greater entropy at elevated temperatures without sacrificing Pd-Pd bonding.

4. CONCLUSIONS

Using PdBi as an illustrative example, we have shown how incommensurability can arise as an entropically-favored structural arrangement at higher temperatures. We began by uncovering the temperature-dependent forms of PdBi: a room-temperature commensurate superstructure of the TlI type that becomes incommensurate at ~200 °C. We followed this with theoretical investigation of the polymorphs, where comm-PdBi is favored by the 18–*n* rule and guided by the CP relief of the major Pd-Bi tensions. The emergence of incomm-PdBi at higher temperatures can also be understood with the CP scheme: breaking the pattern of Pd dimers to form a slab of the TlI-type parent structure increases vibrational freedom in that region of the structure without propagation of CP tensions elsewhere. The **q**-vector's alignment with the *a*-axis is also a direct consequence of the CP scheme, which shows that tilting **q** would lead to enhanced strain on the unpaired Pd atoms at the cores of the TlI-type slabs.

It will be interesting to see how this picture of entropy-driven modulations on a commensurate superstructure might apply to other TlI-type phases and intermetallics more broadly. For example, we might investigate the role of entropy on the structurally related compound AuIn,[23] which also exhibits temperature-dependent modulated polymorphs of the TlI type. In particular, the different nature of the modulations in AuIn (stacking disorder along *b* and positional disorder along *c*), may be related to electronic requirements distinct from those of PdBi due to their different valence electron counts (14 vs. 15 electrons per formula unit). Furthermore, we might consider how the structural behavior of PdBi and AuIn might enable us to predict similar behavior in other TlI-type compounds whose structures have not been completely characterized. More generally, this mechanism could also play a role in lock-in phenomena of other systems, in which incommensurate **q**-vectors are seen to snap to commensurate values at low T.

In fact, the features of PdBi's structural chemistry (electronically-driven, CP-guided phase transitions) align well with a broader guideline that was recently described, called the Frustrated and Allowed Structural Transitions (FAST) principle:[26] complex structural behavior, such as phase transitions and incommensurability, are more likely to occur when the atomic packing and electronic factors work together and less experimentally realizable when the factors are in competition. Here, then, we see comm-PdBi emerge as an allowed structural transition, where both CP relief and the ideal 18–*n* prescription guide the formation of the superstructure. Unlike rigid, 3-dimensional networks of positive CPs ($PtGa_2$[24]) or paths of facile motion outlined by CP quadrupoles (Fe_2Al_5[73] and the Nowotny Chimney Ladders[74]), however, the weakly-coordinated, 2-dimensional CP networks of PdBi provide an interesting setting for entropy-driven structural phenomena: the occurrence of monomer-type defects is allowed. We are looking forward to seeing what other structural paths can be opened in the diverse topologies of CP networks offered by intermetallic chemistry.

ASSOCIATED CONTENT

Supporting Information. Additional synthetic details; Compositional analysis from energy dispersive X-ray spectroscopy; Derivation of the (3+1)D superspace group of comm-PdBi; Origin of the monoclinic distortion; Crystallographic details of comm-PdBi and incomm-PdBi; Computational details; Band structures of TlI-type PdBi and comm-PdBi; DOS distributions calculated with GGA-DFT and the calibrated Hückel method; DOS distributions calculated with and without spin-orbit coupling; Additional raMO analysis of PdBi; CP schemes calculated at different ionicities; CP schemes calculated with and without spin-orbit coupling for TlI-type PdBi.

AUTHOR INFORMATION

Corresponding Authors

*E-mail: sven.lidin@chem.lu.se, danny@chem.wisc.edu

Author Contributions

◊LCF and HMW contributed equally.

ACKNOWLEDGMENTS

We kindly acknowledge all staff of the I19 beamline at Synchrotron Diamond, especially Harriott Nowell and Mark Warren. Also, we thank Hossein Sina for his help with running the DSC. We thank Axel Persson from Lund University for swift and detailed EDX measurements. Furthermore, we are indebted to the Swedish Research Council (Vetenskapsrådet) (SL), Westlings Minnesfond (LCF, Grant 2015-05227) and The Royal Physiographic Society of Lund (LCF/SL, Application No.: 38572). HMW thanks the National Science Foundation for a graduate student fellowship (DGE-1747503). We also gratefully acknowledge the support of NSF Grant DMR-1809594. This work includes calculations that used computing resources supported by NSF Grant CHE-0840494.

REFERENCES

(1) van Smaalen, S.; George, T. F. Determination of the Incommensurately Modulated Structure of α-uranium Below 37 K. *Phys. Rev. B* **1987**, *35*, 7939-7951.

(2) Katkanant, V.; Edwardson, P. J.; Hardy, J. R.; Boyer, L. L. First-Principles Theoretical Explanation of Incommensurate Behavior in Rb_2ZnCl_4. *Phys. Rev. Lett.* **1986**, *57*, 2033-2036.

(3) Ling, C. D.; Schmid, S.; Blanchard, P. E. R.; Petříček, V.; McIntyre, G. J.; Sharma, N.; Maljuk, A.; Yaremchenko, A. A.; Kharton, V. V.; Gutmann, M.; Withers, R. L. A (3 + 3)-Dimensional "Hypercubic" Oxide-Ionic Conductor: Type II Bi_2O_3–Nb_2O_5. *Journal of the American Chemical Society* **2013**, *135*, 6477-6484.

(4) Palatinus, L.; Klementová, M.; Dřínek, V.; Jarošová, M.; Petříček, V. An Incommensurately Modulated Structure of η′-Phase of $Cu_{3+x}Si$ Determined by Quantitative Electron Diffraction Tomography. *Inorg. Chem.* **2011**, *50*, 3743-3751.

(5) Yan, H.; Zhang, Y.; Xu, N.; Senyshyn, A.; Brokmeier, H.-G.; Esling, C.; Zhao, X.; Zuo, L. Crystal Structure Determination of Incommensurate Modulated Martensite in Ni–Mn–In Heusler Alloys. *Acta Mater.* **2015**, *88*, 375-388.

(6) Jiang, J. C.; Schosnig, M.; Schaper, A. K.; Ganster, K.; Rager, H.; Tóth, L. Modulations in Incommensurate $(Ca_{1-x}Sr_x)_2MgSi_2O_7$ Single Crystals. *Phys. Chem. Miner.* **1998**, *26*, 128-134.

(7) Schaper, A. K.; Schosnig, M.; Kutoglu, A.; Treutmann, W.; Rager, H. Transition from the Incommensurately Modulated Structure to the Lock-in Phase in Co-åkermanite. *Acta Crystallogr. B* **2001**, *57*, 443-448.

(8) Kenichi, T.; Kyoko, S.; Hiroshi, F.; Mitsuko, O. Modulated Structure of Solid Iodine During Its Molecular Dissociation Under High Pressure. *Nature* **2003**, *423*, 971-974.

(9) Schoenleber, A. Organic molecular compounds with modulated crystal structures. *Z. Kristallog. – Cryst. Mater.* **2011**, *226*, 499.

(10) Lovelace, J. J.; Murphy, C. R.; Daniels, L.; Narayan, K.; Schutt, C. E.; Lindberg, U.; Svensson, C.; Borgstahl, G. E. O. Protein crystals can be incommensurately modulated. *J. Appl. Crystallogr.* **2008**, *41*, 600-605.

(11) Porta, J.; Lovelace, J.; Borgstahl, G. Supercell approximation for an incommensurately modulated crystal of profilin:actin. *Acta Crystallographica Section A Foundations of Crystallography* **2011**, *67*, C807-C807.

(12) Wu, L.; Meng, Q.; Jooss, C.; Zheng, J.-C.; Inada, H.; Su, D.; Li, Q.; Zhu, Y. Origin of Phonon Glass–Electron Crystal Behavior in Thermoelectric Layered Cobaltate. *Adv. Funct. Mater.* **2013**, *23*, 5728-5736.

(13) Dijkstra, E.; Janner, A.; Meekes, H. The dielectric tensor in incommensurately modulated crystal phases. *J. Phys.: Condens. Matter* **1992**, *4*, 693-713.

(14) de Wolff, P. M. The Pseudo-Symmetry of Modulated Crystal Structures. *Acta Crystallogr. A* **1974**, *30*, 777-785.

(15) Wilson, J. A.; Di Salvo, F. J.; Mahajan, S. Charge-density waves and superlattices in the metallic layered transition metal dichalcogenides. *Adv. Phys* **1975**, *24*, 117-201.

(16) Briggs, A.; Monceau, P.; Nunez-Regueiro, M.; Peyrard, J.; Ribault, M.; Richard, J. Charge density wave formation, superconductivity and Fermi surface determination in $NbSe_3$: a pressure study. *J. Phys. C: Solid State Phys.* **1980**, *13*, 2117-2130.

(17) Grüner, G. The dynamics of charge-density waves. *Rev. Mod. Phys.* **1988**, *60*, 1129-1181.

(18) Sandenaw, T. A. Incommensurate/commensurate charge-density-wave states as a source for plutonium metal behavior. *Phase Transit.* **1989**, *18*, 11-33.

(19) Samulon, E. C.; Islam, Z.; Sebastian, S. E.; Brooks, P. B.; McCourt, M. K.; Ilavsky, J.; Fisher, I. R. Low-temperature structural phase transition and incommensurate lattice modulation in the spin-gap compound $BaCuSi_2O_6$. *Phys. Rev. B* **2006**, *73*, 100407.

(20) Bindi, L. Commensurate-incommensurate Phase Transition in Muthmannite, $AuAgTe_2$: First Evidence of a Modulated Structure at Low Temperature. *Philosophical Magazine Letters* **2008**, *88*, 533-541.

(21) Samson, S. Crystal Structure of $NaCd_2$. *Nature* **1962**, *195*, 259-262.

(22) Samson, S. The crystal structure of the phase β-Mg_2Al_3. *Acta Crystallogr.* **1965**, *19*, 401-413.

(23) Folkers, L. C.; Simonov, A.; Wang, F.; Lidin, S. The Mystery of the AuIn 1:1 Phase and Its Incommensurate Structural Variations. *Inorg. Chem.* **2018**, *57*, 2791-2796.

(24) Mitchell Warden, H. E.; Voyles, P. M.; Fredrickson, D. C. Paths to Stabilizing Electronically Aberrant Compounds: A Defect-Stabilized Polymorph and Constrained Atomic Motion in $PtGa_2$. *Inorg. Chem.* **2018**, *57*, 13880-13894.

(25) Oliynyk, A. O.; Gaultois, M. W.; Hermus, M.; Morris, A. J.; Mar, A.; Brgoch, J. Searching for Missing Binary Equiatomic Phases: Complex Crystal Chemistry in the Hf–In System. *Inorg. Chem.* **2018**, *57*, 7966-7974.

(26) Mitchell Warden, H. E.; Fredrickson, D. C. Frustrated and Allowed Structural Transitions: The Theory-Guided Discovery of the Modulated Structure of IrSi. *J. Am. Chem. Soc.* **2019**, *141*, 19424-19435.

(27) Zhuravlev, N. N. Structure of Superconductors, X. Thermal, Microscopic, and X-ray Investigation of the Bismuth-Palladium System. *J. Exp. Theor. Phys.* **1957**, *5*, 1064-1072.

(28) Bhatt, Y. C.; Schubert, K. Kristallstruktur von PdBi.r. *J. Less Common Met.* **1979**, *64*, 17-24.

(29) Xu, H.; Yan, B.; Zhang, K.; Wang, J.; Li, S.; Wang, C.; Du, Y.; Yang, P.; Jiang, S.; Song, S. N-doped Graphene-supported Binary PdBi Networks for Formic Acid Oxidation. *Appl. Surf. Sci.* **2017**, *416*, 191-199.

(30) Okawa, K.; Kanou, M.; Katagiri, T.; Kashiwaya, H.; Kashiwaya, S.; Sasagawa, T. Crystal Growth and Physical Properties of the Noncentrosymmetric Superconductor PdBi. *Phys. Procedia* **2013**, *45*, 101-104.

(31) Krüger, H.; Kahlenberg, V. Incommensurately modulated ordering of tetrahedral chains in $Ca_2Fe_2O_5$ at elevated temperatures. *Acta Crystallogr. B* **2005**, *61*, 656-662.

(32) Lazic, B.; Krüger, H.; Kahlenberg, V.; Konzett, J.; Kaindl, R. Incommensurate structure of $Ca_2Al_2O_5$ at high temperatures - structure

investigation and Raman spectroscopy. *Acta Crystallogr. B* **2008**, *64*, 417-425.
(33) Yannello, V. J.; Fredrickson, D. C. Orbital Origins of Helices and Magic Electron Counts in the Nowotny Chimney Ladders: the 18 – *n* Rule and a Path to Incommensurability. *Inorg. Chem.* **2014**, *53*, 10627-10631.
(34) Yannello, V. J.; Fredrickson, D. C. Generality of the 18 – *n* Rule: Intermetallic Structural Chemistry Explained through Isolobal Analogies to Transition Metal Complexes. *Inorg. Chem.* **2015**, *54*, 11385-11398.
(35) Fredrickson, D. C. Electronic Packing Frustration in Complex Intermetallic Structures: The Role of Chemical Pressure in Ca_2Ag_7. *Journal of the American Chemical Society* **2011**, *133*, 10070-10073.
(36) Engelkemier, J.; Berns, V. M.; Fredrickson, D. C. First-Principles Elucidation of Atomic Size Effects Using DFT-Chemical Pressure Analysis: Origins of $Ca_{36}Sn_{23}$'s Long-Period Superstructure. *J. Chem. Theory Comput.* **2013**, *9*, 3170-3180.
(37) Berns, V. M.; Engelkemier, J.; Guo, Y.; Kilduff, B. J.; Fredrickson, D. C. Progress in Visualizing Atomic Size Effects with DFT-Chemical Pressure Analysis: From Isolated Atoms to Trends in AB_5 Intermetallics. *J. Chem. Theory Comput.* **2014**, *10*, 3380-3392.
(38) Hilleke, K. P.; Fredrickson, D. C. Discerning Chemical Pressure amidst Weak Potentials: Vibrational Modes and Dumbbell/Atom Substitution in Intermetallic Aluminides. *J. Phys. Chem. A* **2018**, *122*, 8412-8426.
(39) Agilent. *CrysAlis PRO*. Agilent Technologies Ltd, Yarnton, Oxfordshire, England. **2014**.
(40) Palatinus, L.; Chapuis, G. SUPERFLIP - a computer program for the solution of crystal structures by charge flipping in arbitrary dimensions. *J. Appl. Crystallogr.* **2007**, *40*, 786-790.
(41) Petříček, V.; Dušek, M.; Palatinus, L. Crystallographic Computing System JANA2006: General features. *Z. Kristallog. – Cryst. Mater.* **2014**, *229*, 345-352.
(42) Yannello, V. J.; Kilduff, B. J.; Fredrickson, D. C. Isolobal Analogies in Intermetallics: The Reversed Approximation MO Approach and Applications to $CrGa_4$- and Ir_3Ge_7-Type Phases. *Inorg. Chem.* **2014**, *53*, 2730-2741.
(43) Perdew, J. P.; Burke, K.; Ernzerhof, M. Generalized Gradient Approximation Made Simple. *Phys. Rev. Lett.* **1996**, *77*, 3865-3868.
(44) Perdew, J. P.; Burke, K.; Ernzerhof, M. Generalized Gradient Approximation Made Simple [Phys. Rev. Lett. 77, 3865 (1996)]. *Phys. Rev. Lett.* **1997**, *78*, 1396-1396.
(45) Kresse, G.; Hafner, J. Ab initio molecular dynamics for liquid metals. *Phys. Rev. B* **1993**, *47*, 558-561.
(46) Kresse, G.; Hafner, J. Ab initio molecular-dynamics simulation of the liquid-metal--amorphous-semiconductor transition in germanium. *Phys. Rev. B* **1994**, *49*, 14251-14269.
(47) Kresse, G.; Furthmüller, J. Efficient iterative schemes for ab initio total-energy calculations using a plane-wave basis set. *Phys. Rev. B* **1996**, *54*, 11169-11186.
(48) Kresse, G.; Furthmüller, J. Efficiency of ab-initio total energy calculations for metals and semiconductors using a plane-wave basis set. *Comput. Mater. Sci* **1996**, *6*, 15-50.
(49) Blöchl, P. E. Projector augmented-wave method. *Phys. Rev. B* **1994**, *50*, 17953.
(50) Kresse, G.; Joubert, D. From ultrasoft pseudopotentials to the projector augmented-wave method. *Phys. Rev. B* **1999**, *59*, 1758-1775.
(51) Stacey, T. E.; Fredrickson, D. C. Perceiving Molecular Themes in the Structures and Bonding of Intermetallic Phases: The Role of Hückel Theory in an *ab initio* Era. *Dalton Trans.* **2012**, *41*, 7801-7813.
(52) Landrum, G. A.; Glassey, W. V. YAeHMOP: Yet Another Extended Hückel Molecular Orbital Package, YAeHMOP is freely available via the Internet at URL: https://sourceforge.net/projects/yaehmop/.
(53) The MATLAB programs used in the raMO and CP analyses can be obtained by contacting one of the corresponding authors (DCF).
(54) Goedecker, S.; Teter, M.; Hutter, J. Separable dual-space Gaussian pseudopotentials. *Phys. Rev. B* **1996**, *54*, 1703-1710.
(55) Gonze, X.; Beuken, J. M.; Caracas, R.; Detraux, F.; Fuchs, M.; Rignanese, G. M.; Sindic, L.; Verstraete, M.; Zerah, G.; Jollet, F.; Torrent, M.; Roy, A.; Mikami, M.; Ghosez, P.; Raty, J. Y.; Allan, D. C. First-principles computation of material properties: the ABINIT software project. *Comput. Mater. Sci* **2002**, *25*, 478-492.
(56) Gonze, X. A brief introduction to the ABINIT software package. *Z. Kristallog. – Cryst. Mater.* **2005**, *220*, 558-562.
(57) Gonze, X.; Amadon, B.; Anglade, P. M.; Beuken, J. M.; Bottin, F.; Boulanger, P.; Bruneval, F.; Caliste, D.; Caracas, R.; Côté, M.; Deutsch, T.; Genovese, L.; Ghosez, P.; Giantomassi, M.; Goedecker, S.; Hamann, D. R.; Hermet, P.; Jollet, F.; Jomard, G.; Leroux, S.; Mancini, M.; Mazevet, S.; Oliveira, M. J. T.; Onida, G.; Pouillon, Y.; Rangel, T.; Rignanese, G. M.; Sangalli, D.; Shaltaf, R.; Torrent, M.; Verstraete, M. J.; Zerah, G.; Zwanziger, J. W. ABINIT: First-principles approach to material and nanosystem properties. *Comput. Phys. Commun.* **2009**, *180*, 2582-2615.
(58) Hartwigsen, C.; Goedecker, S.; Hutter, J. Relativistic separable dual-space Gaussian pseudopotentials from H to Rn. *Phys. Rev. B* **1998**, *58*, 3641-3662.
(59) Bader, R. F. W. *Atoms in Molecules: A Quantum Theory*; Oxford; New York: Clarendon Press, 1990.
(60) Henkelman, G.; Arnaldsson, A.; Jónsson, H. A fast and robust algorithm for Bader decomposition of charge density. *Comput. Mater. Sci* **2006**, *36*, 354-360.
(61) Sanville, E.; Kenny, S. D.; Smith, R.; Henkelman, G. Improved grid-based algorithm for Bader charge allocation. *J. Comput. Chem.* **2007**, *28*, 899-908.
(62) Tang, W.; Sanville, E.; Henkelman, G. A grid-based Bader analysis algorithm without lattice bias. *J. Phys.: Condens. Matter* **2009**, *21*, 084204.
(63) Oliveira, M. J. T.; Nogueira, F. Generating relativistic pseudo-potentials with explicit incorporation of semi-core states using APE, the Atomic Pseudo-potentials Engine. *Comput. Phys. Commun.* **2008**, *178*, 524-534.
(64) Okamoto, H. The Bi-Pd (Bismuth-Palladium) System. *J. Phase Equilib.* **1994**, *15*, 191-194.
(65) One might notice a weakening of the partial Debye-Scherrer rings in the 200 °C measurement. This originates from a general decrease in intensity of the diffraction pattern at elevated temperature, and (alas) should not be taken as a sign of a general improvement in the sample quality.
(66) The monoclinic distortion away from α = 90° is likely masked by twinning. In this case, the twin domains are balanced, 50:50.
(67) Helmholz, L. The Crystal Structure of the Low Temperature Modification of Thallous Iodide. *Z. Kristallog. – Cryst. Mater.* **1936**, *95*, 129-137.
(68) Peierls, R. E. *Quantum theory of solids*; Clarendon Press: Oxford, 1955.
(69) Pouget, J.-P. The Peierls instability and charge density wave in one-dimensional electronic conductors. *CR Phys* **2016**, *17*, 332-356.
(70) Wu, J.; Gong, Y.; Inoshita, T.; Fredrickson, D. C.; Wang, J.; Lu, Y.; Kitano, M.; Hosono, H. Tiered Electron Anions in Multiple Voids of

LaScSi and Their Applications to Ammonia Synthesis. *Adv. Mater.* **2017**, *29*, 1700924.
(71) Park, S.-W.; Hosono, H.; Fredrickson, D. C. Cation Clustering in Intermetallics: The Modular Bonding Schemes of CaCu and Ca_2Cu. *Inorg. Chem.* **2019**, *58*, 10313-10322.
(72) Engelkemier, J.; Fredrickson, D. C. Chemical Pressure Schemes for the Prediction of Soft Phonon Modes: A Chemist's Guide to the Vibrations of Solid State Materials. *Chem. Mater.* **2016**, *28*, 3171-3183.
(73) Vinokur, A. I.; Hilleke, K. P.; Fredrickson, D. C. Principles of weakly ordered domains in intermetallics: the cooperative effects of atomic packing and electronics in Fe_2Al_5. *Acta Crystallogr. A* **2019**, *75*, 297-306.
(74) Lu, E.; Fredrickson, D. C. Templating Structural Progessions in Intermetallics: How Chemical Pressure Directs Helix Formation in the Nowotny Chimney Ladders. *Inorg. Chem.* **2019**, *58*, 4063-4066.

For Table of Contents Use Only

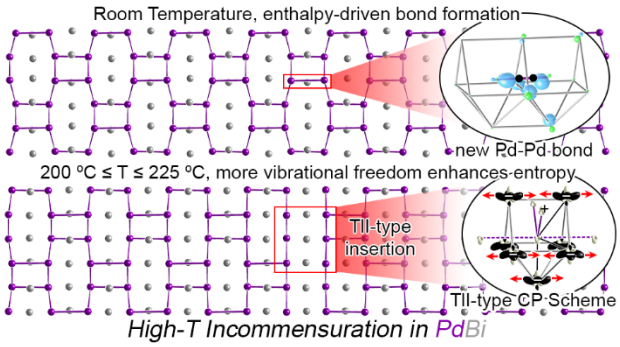

Synopsis: Incommensurate order, in which mismatched periodic patterns combine to make an ordered yet aperiodic structure, is emerging as a general phenomenon in the solid state. Here, we elucidate a modulation in the intermetallic compound PdBi that illustrates how incommensurability can arise from the controlled increase of entropy at elevated temperatures. Such behavior may emerge in other materials when competing electronic states weaken a low-temperature superstructure, and the Chemical Pressure scheme offers paths for accommodating defects.